

This article may be downloaded for personal use only. Any other use requires prior permission of the author and AIP Publishing.

The following article appeared in *Applied Physics Letters* 104, 212401 (2014); and may be found at <https://doi.org/10.1063/1.4879544>

## Enhanced refrigerant capacity in two-phase nanocrystalline/amorphous NdPrFe<sub>17</sub> melt-spun ribbons

C. F. Sánchez-Valdés, P. J. Ibarra-Gaytán, J. L. Sánchez Llamazares, M. Ávalos-Borja, Pablo Álvarez-Alonso, Pedro Gorria, and J. A. Blanco

Citation: *Appl. Phys. Lett.* **104**, 212401 (2014);

View online: <https://doi.org/10.1063/1.4879544>

View Table of Contents: <http://aip.scitation.org/toc/apl/104/21>

Published by the [American Institute of Physics](#)

---

### Articles you may be interested in

[Texture-induced enhancement of the magnetocaloric response in melt-spun DyNi<sub>2</sub> ribbons](#)

*Applied Physics Letters* **103**, 152401 (2013); 10.1063/1.4824073

[Excellent magnetocaloric properties of melt-extracted Gd-based amorphous microwires](#)

*Applied Physics Letters* **101**, 102407 (2012); 10.1063/1.4751038

[Table-like magnetocaloric effect in the Gd-Co-Al alloys with multi-phase structure](#)

*Applied Physics Letters* **104**, 072401 (2014); 10.1063/1.4865554

[Adiabatic magnetocaloric effect in Ni<sub>50</sub>Mn<sub>35</sub>In<sub>15</sub> ribbons](#)

*Applied Physics Letters* **109**, 212402 (2016); 10.1063/1.4968592

[Giant magnetocaloric effect in melt-spun Ni-Mn-Ga ribbons with magneto-multistructural transformation](#)

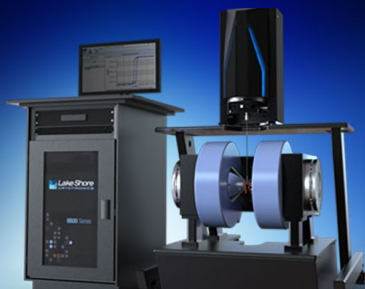
*Applied Physics Letters* **104**, 044101 (2014); 10.1063/1.4863273

[Influence of negative lattice expansion and metamagnetic transition on magnetic entropy change in the compound LaFe<sub>11.4</sub>Si<sub>1.6</sub>](#)

*Applied Physics Letters* **78**, 3675 (2001); 10.1063/1.1375836


---

 **Lake Shore**  
CRYOTRONICS



**8600 Series VSM**

For fast, highly sensitive  
measurement performance

LEARN MORE 

## Enhanced refrigerant capacity in two-phase nanocrystalline/amorphous NdPrFe<sub>17</sub> melt-spun ribbons

C. F. Sánchez-Valdés,<sup>1</sup> P. J. Ibarra-Gaytán,<sup>1</sup> J. L. Sánchez Llamazares,<sup>1,a)</sup>  
 M. Avalos-Borja,<sup>1</sup> Pablo Álvarez-Alonso,<sup>2</sup> Pedro Gorria,<sup>3</sup> and J. A. Blanco<sup>4</sup>

<sup>1</sup>Instituto Potosino de Investigación Científica y Tecnológica, Camino a la Presa San José 2055 Col. Lomas  
 4<sup>a</sup>, San Luis Potosí S.L.P. 78216, Mexico

<sup>2</sup>Departamento de Electricidad y Electrónica, Universidad del País Vasco (UPV/EHU), 48940 Leioa,  
 Spain

<sup>3</sup>Departamento de Física & IUTA, EPI, Universidad de Oviedo, 33203 Gijón, Spain

<sup>4</sup>Departamento de Física, Universidad de Oviedo, Calvo Sotelo s/n, 33007 Oviedo, Spain

(Received 22 February 2014; accepted 8 May 2014; published online 27 May 2014)

The magnetocaloric properties of NdPrFe<sub>17</sub> melt-spun ribbons composed of nanocrystallites surrounded by an intergranular amorphous phase have been studied. The nanocomposite shows two successive second-order magnetic phase transitions (303 and 332 K), thus giving rise to a remarkable broadening ( $\approx 84$  K) of the full-width at the half-maximum of the magnetic entropy change curve,  $\Delta S_M(T)$ , with a consequent enhancement of the refrigerant capacity  $RC$ . For a magnetic field change of 2 T,  $|\Delta S_M^{\text{peak}}| = 2.1 \text{ J kg}^{-1} \text{ K}^{-1}$  and  $RC = 175 \text{ J kg}^{-1}$ . Therefore, the reversible magnetocaloric response together with the one-step preparation process makes these nanostructured Fe-rich alloy ribbons particularly attractive for room temperature magnetic refrigeration. © 2014 AIP Publishing LLC. [<http://dx.doi.org/10.1063/1.4879544>]

The refrigerant capacity  $RC$  is one of the key figures of merit for characterizing the magnetocaloric (MC) response of any material, since it quantifies the amount of heat that might be transferred from the cold to the hot sink through an ideal refrigeration cycle.<sup>1-4</sup> This parameter is usually calculated from the temperature dependence of the magnetic entropy change  $\Delta S_M(T)$  curve and basically depends on its peak or maximum value  $|\Delta S_M^{\text{peak}}|$  and on the temperature width of the curve which is usually quantified by its full-width given. In practice, three different criteria were used to compute the  $RC$ : (a) by finding the product  $|\Delta S_M^{\text{peak}}| \times \delta T_{\text{FWHM}}$  (hereafter referred to as  $RC-1$ ),<sup>1</sup> where  $\delta T_{\text{FWHM}} = T_{\text{hot}} - T_{\text{cold}}$ , corresponds to the full width at half maximum of the  $\Delta S_M(T)$  curve; it is usually assumed that  $\delta T_{\text{FWHM}}$  coincides with the temperature span of the thermodynamic cycle being  $T_{\text{hot}}$  and  $T_{\text{cold}}$  the hot and cold ends, respectively; (b) by calculating the integral under the  $\Delta S_M(T)$  curve between  $T_{\text{hot}}$  and  $T_{\text{cold}}$  ( $RC-2$ );<sup>3</sup> and (c) by maximizing the product  $\Delta S_M \times \delta T$  below the  $\Delta S_M(T)$  curve ( $RC-3$ ).<sup>4</sup> Roughly speaking, a large refrigerant capacity basically depends on having as large  $|\Delta S_M^{\text{peak}}|$  as possible combined with a reasonably broad  $\Delta S_M(T)$  curve.

In ferromagnetic materials two different regions can be observed in the  $\Delta S_M(T)$  curve, i.e., below and above the Curie temperature,  $T_C$ . The maximum of the curve typically appears at  $T \approx T_C$  and its shape has been usually referred as *caret-like* type.<sup>5</sup> The peak is asymmetric and the region below  $T_C$  is usually wider, except in materials with  $T_C$  in the very low temperature range ( $T < 20$  K) and/or those exhibiting field-induced changes of the magnetic structure such as spin-reorientation phenomena. As  $RC$  depends on the two factors mentioned above, it is difficult to enlarge it beyond a

certain limit for a single-phase ferromagnetic material. However, it has been shown that in some cases the appropriate processing of the material may lead to an enhancement of the  $RC$  through the increase of  $\delta T_{\text{FWHM}}$ . Examples of this are the amorphization<sup>6</sup> or nanostructure formation by ball milling,<sup>7-9</sup> and the introduction of atomic disorder by rapid solidification.<sup>10</sup> Then, the alloys produced by those procedures exhibit a broadening of  $\Delta S_M(T)$  curve due to a more gradual decrease of the magnetization as a function of temperature  $M(T)$  curve across the ferro-to-paramagnetic phase transition.

A more effective way of fabricating magnetic refrigerants with enhanced refrigerant capacity due to a wider working temperature span is making a two- or a multi-phase MC composite. Up to now, the main target in this sense has been to obtain a material with a *table-like* MC response, which is the more suitable for the Ericsson-like refrigeration cycle.<sup>11</sup> The first studies on this feature were developed by Hashimoto *et al.*,<sup>12,13</sup> who proposed a three-layered sintered structure based on  $\text{RAI}_2$  Laves phases ( $R = \text{rare earth}$ ). Other early works were carried out by Smaili and Chahine;<sup>14,15</sup> and Korte *et al.*<sup>16</sup> In recent years, a renewed interest in the development of two-component magnetocaloric refrigerants has emerged due to the limitations of single-phase magnetocaloric materials for increasing  $\delta T_{\text{FWHM}}$ .<sup>17</sup> In particular, the search for the essential factors influencing the achievement of a *table-like*  $\Delta S_M(T)$  curve around room temperature, as well as the modeling of such curve, for a two-phase layered composites has been currently a subject of research interest.<sup>18-21</sup> One of the most studied sort of composites is that made of two amorphous melt-spun alloy ribbons in a proper weight fraction having an adequate difference in their  $T_C$  values and similar values of  $|\Delta S_M^{\text{peak}}|$  (i.e., two-independent mounted and stuck ribbon pieces). In this case, the resulting  $\Delta S_M(T)$  curve coincides approximately

<sup>a)</sup> Author to whom correspondence should be addressed. Electronic mail: jose.sanchez@ipicyt.edu.mx

with the weighted superposition of the curves shown by the individual constituents.<sup>18,19,21</sup> Another type of composite, which is of particular interest from the technological point of view, is the one obtained *in-situ* when the chemical composition, synthesis parameters, and/or the processing method combine favorably to form a two-phase or multi-phase magnetic system. If the material shows successive magnetic phase transitions and their  $T_C$  does not differ by too much, an expanded  $\Delta S_M(T)$  curve will be obtained with the consequent  $RC$  enhancement with respect to any of the individual phases. Recently, several *in situ* composite MC materials have been reported in rare-earth-based alloy systems such as GdAlMn,<sup>22</sup> FeGdAl,<sup>23</sup> ErGa,<sup>24</sup> or GdCoAl.<sup>25,26</sup> All of them operate in the low-temperature region (i.e., the magnetic phase transition is below 200 K).

The binary intermetallic compounds  $R_2Fe_{17}$  with  $R = Nd$  or  $Pr$  are collinear ferromagnets with a high saturation magnetization (i.e., 185 and 192 A m<sup>2</sup> kg<sup>-1</sup> at 5 K, respectively), and Curie temperature around room temperature (i.e.,  $285 \pm 5$  and  $335 \pm 5$  K, respectively).<sup>27,28</sup> The interest to consider them as potential candidates for room-temperature magnetic refrigeration lies in their low rare-earth content. Until now, the assessment of their MC properties has been focused on bulk alloys produced by arc melting followed by a prolonged high-temperature thermal annealing (several days in the 1273 - 1373 K temperature range),<sup>7-9,29,30</sup> and powdered ball-milled nanocrystalline alloys.<sup>7-9</sup> In nanometer-sized  $R_2Fe_{17}$  ( $R = Nd$  or  $Pr$ ) powders produced by severe mechanical milling of single-phase bulk alloys, a moderate decrease in  $|\Delta S_M^{peak}|$  together with the enlargement of both,  $\delta T_{FWHM}$  and  $RC$ , has already been reported.<sup>7-9</sup>

As far as we know, the MC response of 2:17 melt-spun compounds with light R elements has not been explored yet. However, a few years ago, Fang *et al.* synthesized single-phase microcrystalline ribbons of the isostructural  $Y_2Fe_{17}$  compound at different copper wheel speeds (from 10 to 40 ms<sup>-1</sup>; average grain  $\langle d \rangle$  ranging from around 1  $\mu m$  to 250 nm) and studied their MC behavior.<sup>31</sup> The samples crystallized into the hexagonal  $Th_2Ni_{17}$ -type structure; the largest  $\Delta S_M^{peak}$  was found for the ribbons prepared at a wheel speed of 20 ms<sup>-1</sup> (i.e.,  $-1.89$  J kg<sup>-1</sup> K<sup>-1</sup> for a magnetic field change  $\mu_0 \Delta H = 1$  T).

In this Letter, we report on the microstructure, magnetic behavior, and magnetocaloric response of pseudo-binary NdPrFe<sub>17</sub> melt-spun ribbons. The resulting MC properties are compared with those reported for the bulk parent compound Pr<sub>2</sub>Fe<sub>17</sub> to emphasize on the improved refrigerant capacity and working temperature range of the fabricated alloy ribbons.

The ribbons, with nominal composition NdPrFe<sub>17</sub>, were produced by rapid solidification using a homemade melt spinning setup at a wheel (copper) linear speed of 20 ms<sup>-1</sup> from bulk pellets previously produced by arc melting. As raw materials, pure metallic elements were used ( $\geq 99.9\%$ ). Both the arc melted starting alloys and the melt-spun ribbons were obtained under a highly pure Ar atmosphere.

X-ray diffraction (XRD) patterns of finely powdered ribbon samples were collected with a Bruker AXS model D8 Advance X-ray powder diffractometer using Cu-K<sub>α</sub> radiation

( $\lambda = 1.5418 \text{ \AA}$ ;  $20^\circ \leq 2\theta \leq 100^\circ$ ; step increment  $0.01^\circ$ ). The Rietveld analysis of the diffraction data was carried out with the FULLPROF suite package.<sup>32</sup> Microstructure and elemental composition were investigated using a Helios FEI Dual beam Helios Nanolab FIB scanning electron microscope (SEM) equipped with an energy dispersive spectroscopy (EDS) system. SEM images were taken on the cross-section of cleaved ribbon samples; the granular microstructure of many ribbons was analyzed. The images showing the nanostructure of the samples were collected in a FEI Tecnai<sup>TM</sup> high-resolution transmission electron microscope (HRTEM). For TEM examination a tiny amount of finely grounded ribbons were put into a vial with ethanol. The vial was sonicated in an ultrasonic bath for 10 min to form a suspension. A drop of the upper part of the suspension was applied to a copper grid that was dried in air.

Magnetic measurements were performed by vibrating sample magnetometry in a Quantum Design PPMS<sup>®</sup> EverCool<sup>®</sup>-9 T platform. The magnetic field  $\mu_0 H$  was applied along the ribbon axis (i.e., the rolling direction) to minimize the demagnetizing field effect. The low-field (5 mT) and high-field (5 T) magnetization as a function of temperature,  $M(T)$ , curves were measured between 100 and 400 K. The magnetic transition temperatures were obtained from the minimum of the  $dM/dT(T)$  curve measured under  $\mu_0 H = 5$  mT. In order to determine the  $\Delta S_M(T)$  curve from numerical integration of the Maxwell relation (i.e.,  $\Delta S_M(T, \mu_0 H) = \mu_0 \int_0^{\mu_0 H_{max}} \left[ \frac{\partial M(T, \mu_0 H')}{\partial T} \right]_{\mu_0 H} dH'$ ), a set of isothermal magnetization curves,  $M(\mu_0 H)$ , was measured in the temperature range of 200–400 K with a  $\Delta T$  step of 5 K up to a maximum applied magnetic field of 2 T. With the aim of minimizing the error in the calculation of  $\Delta S_M$ , the magnetization was measured for a large number of selected values of  $\mu_0 H$  at each temperature. The values of  $RC-1$ ,  $RC-2$ , and  $RC-3$  were obtained from the criteria stated above.

The EDS analyses (not shown) performed on the ribbon cross-section and on both surfaces revealed that the starting chemical composition, namely, NdPrFe<sub>17</sub>, was well reproduced in the as-quenched (aq) samples. Figure 1(a) shows the experimental powder XRD pattern together with the fit to the superposition of the XRD structural profiles corresponding to the rhombohedral  $Th_2Zn_{17}$ -type crystal structure with space group  $R\bar{3}m$  and unit cell parameters  $a = 8.553(3) \text{ \AA}$  and  $c = 12.543(1) \text{ \AA}$  [cell volume  $V = 794.7(1) \text{ \AA}^3$ ] and bcc  $\alpha$ -Fe as an impurity phase (the more intense Bragg reflection of this phase is indicated in the graph by a vertical arrow). The reliability parameters obtained from the Rietveld refinement of the pattern ( $R_p = 10.2\%$ ,  $R_{wp} = 13.0\%$ ,  $R_{exp} = 8.1\%$ ,  $\chi^2 = 2.6\%$ , and  $R_B = 6.6\%$ ) indicate that the fit is reasonably good, although the calculated intensity for the peaks below  $2\theta = 50^\circ$  is lower than the one observed. The latter is a direct consequence of the existence of a disordered intergranular phase that contributes to the XRD pattern background in this region (a typical amorphous halo can be perceived within the  $35^\circ$ – $50^\circ$   $2\theta$ -range below the intensity peaks belonging to the major 2:17 crystalline phase). Moreover, we have estimated the mean crystalline size from the broadening of the intensity peaks to be about 20 nm. The ribbons produced contain 96(2) wt. % of the 2:17 phase, together with 4(2) wt. % of

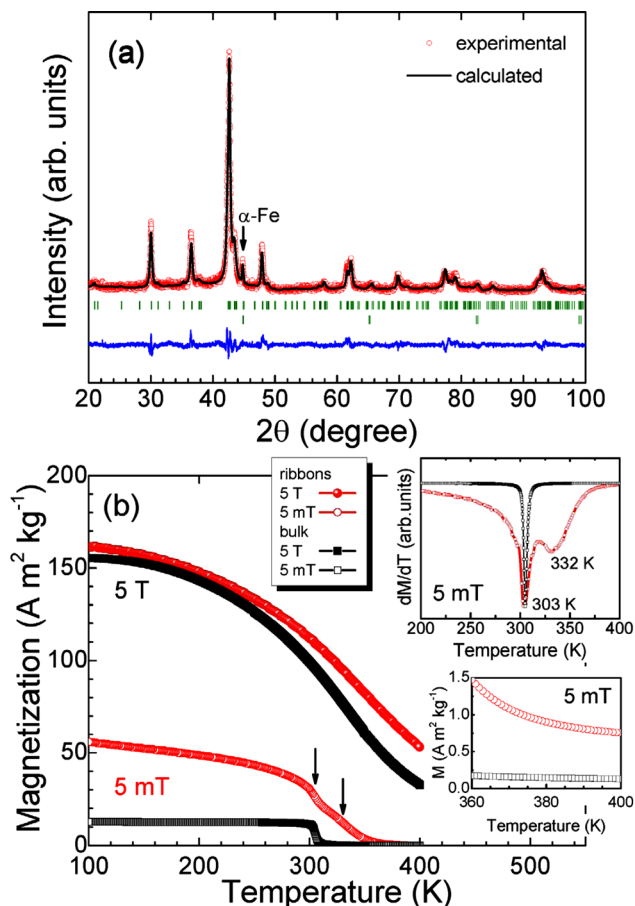


FIG. 1. (a) Experimental (red circles) and calculated (black line) X-ray powder diffraction pattern for as-quenched (aq) NdPrFe<sub>17</sub> alloy ribbons (Cu-K<sub>α</sub> radiation). The difference between both patterns is depicted at the bottom of the figure. The second series of vertical green bars corresponds to the crystal structure of the impurity  $\alpha$ -Fe phase ( $\sim 4$  wt. %); the vertical arrow points to its more intense Bragg reflection. (b) Temperature dependence of magnetization measured under static magnetic field values of 5 mT and 5 T for NdPrFe<sub>17</sub> ribbons (red circles) and bulk samples (black squares). The vertical arrows point to the magnetic transition of the 2:17 rhombohedral phase and the secondary amorphous phase. Top inset:  $dM/dT$  vs.  $T$  curve at 5 mT. Bottom inset: low-field  $M(T)$  curves between 360 K and 400 K.

$\alpha$ -Fe. This amount of  $\alpha$ -Fe is similar to the one determined in bulk R<sub>2</sub>Fe<sub>17</sub> (R = Nd, Pr) alloys but well below the one found in ball-milled nanostructured powders (typically  $\geq 8$  wt. %).<sup>7–9</sup> It is worth noting that the 2:17 crystalline phase is obtained directly from the rapid solidification process as a major phase, in contrast with bulk R<sub>2</sub>Fe<sub>17</sub> (R = Nd, Pr) alloys that require a long-term heat treatment during several days at temperatures around 1273 K or higher for a complete homogenization of the 2:17 crystalline structure.<sup>7–9,29,30</sup> Consequently, melt-spinning offers a significant advantage regarding the processing conditions of these MC alloys.

Figure 1(b) shows the temperature dependencies of the magnetization  $M(T)$  for the aq ribbons measured under low- and high-static magnetic field values of 5 mT and 5 T. In the same graph, we plot the corresponding curves for a single-phase bulk alloy with the same nominal composition. The NdPrFe<sub>17</sub> bulk sample was fabricated by arc melting the pure metallic elements followed by annealing at 1373 K in a vacuumed quartz ampoule for 1 week. The phase composition along with the lattice parameters for the 2:17 structure determined for this sample from the Rietveld refinement of

the XRD pattern were similar to those determined for melt-spun ribbons. The sample contained a small amount of residual  $\alpha$ -Fe of  $\sim 4$  wt. %, and the lattice constants obtained for the 2:17 structure were  $a = 8.557(3)$  Å and  $c = 12.452(1)$  Å (cell volume  $V = 792.5(1)$  Å<sup>3</sup>). The  $dM/dT$  vs.  $T$  curves in the immediacy of the magnetic transition for both ribbon and bulk samples are plotted in the top right inset. In contrast with the bulk alloy, which exhibits a single and sharp magnetic phase transition at  $T_C \approx 304$  K, the low-field  $M(T)$  curve for the ribbons shows two successive magnetic transitions (as a result of which, the high-field curve spreads out over a wider temperature interval in the magnetic transition region). The primary at  $T_C \approx 303$  K almost coincides with the magnetic transition measured for the bulk sample, and therefore, we may ascribe it to the 2:17 crystalline phase. However, a minor second transition is observed at  $T_C \approx 332$  K. The low-field  $M(T)$  curves for both melt-spun and bulk samples in the temperature range between 360 and 400 K are shown in the bottom right inset of Figure 1(b); in agreement with the presence of a small amount of bcc  $\alpha$ -Fe in both samples they do not reach zero magnetization value.

In order to clarify the origin of this secondary magnetic phase, which shows a higher  $T_C$  than the 2:17 crystalline phase, the ribbons were examined by scanning and transmission electron microscopy. Figure 2(a) and its inset show typical low-magnification SEM micrographs of the ribbons cross-section. From these images, we can estimate that the ribbon thickness is around 20  $\mu$ m and also that the ribbon morphology consists of different shaped entities with average size of tens of nanometers. Furthermore, the TEM

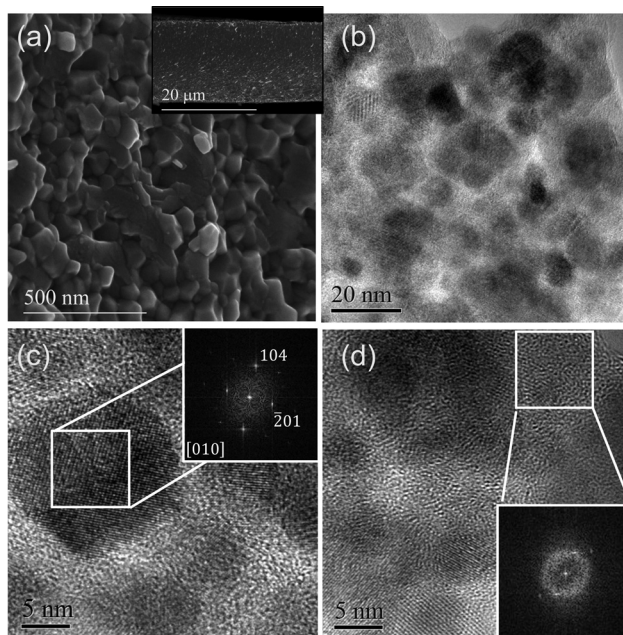


FIG. 2. (a) Typical SEM micrographs of the ribbons cross-section. (b)–(d) Transmission electron images of the alloy ribbons collected at different magnifications. In (c), a high resolution TEM image shows the lattice planes of a 2:17 nanograin; the Fourier transform of the square indicated area is shown in the inset. The spots are indexed according to the structure used for Rietveld refinement of Fig. 1. High-resolution image shows that nanoparticles are surrounded by a disordered (amorphous) intergranular phase; the corresponding Fourier transform of the square is shown in the inset of the image.

micrograph in Figure 2(b) indicates that these “nano-entities” are composed of smaller agglomerated nanocrystals with an average grain size that varies between 7 and 15 nm. In addition, note that those nanocrystals are surrounded by light-gray intergranular phase. The HRTEM images illustrated in Figures 2(c) and 2(d) give a more detailed view of the morphology at the nanometer length scale. As Figure 2(c) shows, the dark granular regions observed in Figure 2(b) are individual nanocrystalline grains for which well-defined lattice planes can be observed. The selected areas Fourier transform patterns for both regions (shown in the insets) further confirm the amorphous nature of the intergranular region as well as the crystallinity of the nanograins. The Fourier transform shown in the inset of Fig. 2(c) identifies a NdPrFe<sub>17</sub> crystal in [010] orientation. In contrast, Figure 2(d) puts in evidence the atomic disorder of the intergranular phase. Hence, a two-phase magnetic nanocomposite system is formed in the ribbons due to the fast solidification procedure and consists of NdPrFe<sub>17</sub> nanocrystals surrounded by a thin intergranular amorphous phase, as it was previously presumed from the XRD pattern analysis.

The minimum in the  $dM/dT(T)$  curve [see inset of Fig. 1(b)] coincides with the  $T_C$  of the 2:17 phase of the bulk NdPrFe<sub>17</sub> samples fabricated (i.e., the average value of  $T_C$  remains unchanged), but the magnetic transition is considerably broader, in a similar way to that already observed in nanostructured R<sub>2</sub>Fe<sub>17</sub> (R = Nd, Pr) powders.<sup>7–9</sup> This broadening of the primary magnetic transition, which corresponds to the 2:17, is attributed to the large number of grain boundaries due to nanostructuring as in the case of nanostructured ball-milled powders. The local environments of Fe atoms slightly change at the grain boundaries, thus modifying the Fe-Fe magnetic interactions and giving rise to a distribution of Curie temperature values. In a recent report, we correlated the  $\Delta S_M(T)$  curve broadening with the  $T_C$  distribution in nanostructured R<sub>2</sub>Fe<sub>17</sub> (R = Nd, Pr) powders.<sup>33</sup> As in 2:17 compounds, the Curie temperature is mainly determined by Fe-Fe interatomic distances, the similar  $T_C$  value found for the 2:17 phase in both samples is consistent with the small unit cell volume change between both samples ( $\Delta V/V \sim 0.3\%$ ).

Figure 3(a) compares the  $\Delta S_M(T)$  curves obtained under magnetic field changes of 1.5 and 2 T for the NdPrFe<sub>17</sub> ribbons with those reported for bulk polycrystalline Pr<sub>2</sub>Fe<sub>17</sub> alloy,<sup>8</sup> while the normalized  $\Delta S_M(T)/\Delta S_M^{\text{peak}}$  versus  $T/T_C$  curves at 1.5 T for both samples are depicted in the inset. The magnetocaloric properties of both materials are outlined in Table I. Note that NdPrFe<sub>17</sub> ribbons exhibit a lower  $\Delta S_M^{\text{peak}}$  (that is located at the  $T_C$  of the 2:17 phase) along with a substantially broader  $\Delta S_M(T)$  curve. The normalized  $\Delta S_M(T)/\Delta S_M^{\text{peak}}$  versus  $T/T_C$  curves reveal that the broadening results from the enlargement of the curve at both regions below and above the  $T_C$  of the crystalline phase, as a consequence of the distribution of  $T_C$  values in the intergranular amorphous phase [see inset in Fig. 1(b)].

Figure 3(b) shows the dependence of the refrigerant capacities  $RC-1$ ,  $RC-2$ , and  $RC-3$  and the temperatures  $T_{\text{cold}}$  and  $T_{\text{hot}}$  (inset) upon the magnetic field change for the composite ribbons. Note that despite ribbon samples exhibit a lower  $\Delta S_M^{\text{peak}}$ , for a magnetic field change of 2 T (which is

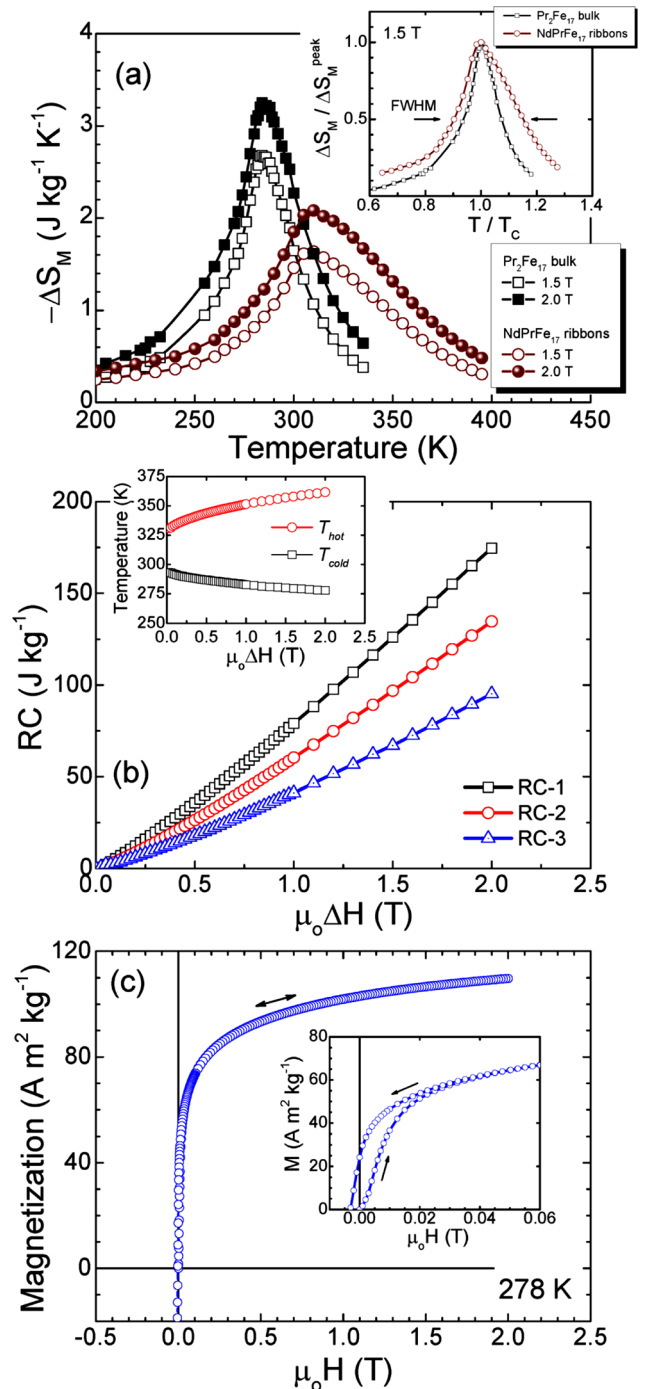


FIG. 3. (a) Temperature dependence of the magnetic entropy change  $\Delta S_M(T)$  under magnetic field changes of 1.5 and 2 T for as-quenched NdPrFe<sub>17</sub> alloy ribbons. For the sake of comparison, the curves corresponding to a polycrystalline Pr<sub>2</sub>Fe<sub>17</sub> bulk alloy are also plotted.<sup>8</sup> Inset: normalized temperature dependence of the magnetic entropy change as a function of  $T/T_C$  for NdPrFe<sub>17</sub> alloy ribbons and bulk Pr<sub>2</sub>Fe<sub>17</sub> alloy. The horizontal arrows indicate the full-width at half-maximum of the curves. (b) Field dependence of the refrigerant capacities  $RC-1$ ,  $RC-2$ , and  $RC-3$  for NdPrFe<sub>17</sub> ribbons. Inset: field dependence of the temperatures  $T_{\text{hot}}$  and  $T_{\text{cold}}$  that define the  $\delta T_{\text{FWHM}}$ . (c) Initial and demagnetization curves measured at 278 K up to  $\mu_0H = 2$  T. Inset: low-field region of the hysteresis loop.

the reference value for a practical refrigeration system) they exhibit a sizeable refrigerant capacity in the room temperature range that is over the one found in bulk Pr<sub>2</sub>Fe<sub>17</sub> alloys (i.e., an increase in  $RC-1$  and  $RC-2$  of  $\sim 17\%$  and  $\sim 12\%$ , respectively, is found); this is due to the enlargement (a 78% higher) of the working temperature range that embraces the

TABLE I. Maximum magnetic entropy change  $|\Delta S_M^{\text{peak}}|$ , useful working temperature range ( $\delta T_{\text{FWHM}} = T_{\text{hot}} - T_{\text{cold}}$ ), and refrigerant capacity for a magnetic field change of 1.5 and 2.0 T for aq NdPrFe<sub>17</sub> alloy ribbons compared to the reported values for bulk Pr<sub>2</sub>Fe<sub>17</sub> alloy.<sup>8</sup>

Sample	$T_C$ (K)	$\mu_0\Delta H$ (T)	$ \Delta S_M^{\text{peak}} $ (J kg <sup>-1</sup> K <sup>-1</sup> )	$T_{\text{cold}}$ (K)	$T_{\text{hot}}$ (K)	$\delta T_{\text{FWHM}}$ (K)	$RC-1$ (J kg <sup>-1</sup> )	$RC-2$ (J kg <sup>-1</sup> )
NdPrFe <sub>17</sub> aq ribbons	303	1.5	1.6	280	357	77	126	97
		2.0	2.1	278	362	84	175	135
Pr <sub>2</sub> Fe <sub>17</sub> bulk	285	1.5	2.6	265	305	40	105	80
		2.0	3.2	263	310	47	150	110

room temperature interval. The latter results from the two successive second-order transition effect and causes the  $RC$  enlargement. It must be also noted that  $\delta T_{\text{FWHM}}$  is superior to other magnetic refrigerants in the room-temperature range including the benchmark MC material Gd ( $\delta T_{\text{FWHM}}$  for Gd is typically  $\sim 40$ – $45$  K).<sup>1,2,34</sup> Finally, it must be emphasized that the reversible character of the magnetocaloric effect was confirmed by measuring the hysteresis loop of ribbon samples at  $T_{\text{cold}}$  (i.e., 278 K). The initial and demagnetization  $M(\mu_0H)$  curves from the first- to third-quadrant are shown in Fig. 3(c); the inset zooms into the low-field region of the hysteresis loop. The sample shows an intrinsic coercivity  $\mu_0H_C$  of 3 mT, a remanence-to-saturation ratio of 0.2 and a negligible hysteresis loss at this temperature ( $0.007$  J kg<sup>-1</sup>; given by the area enclosed between the virgin and demagnetization curve in the first quadrant). Hence, within the operating temperature range  $\delta T_{\text{FWHM}}$ , no significant hysteresis losses were measured in agreement with the second-order character of the phase transitions. As a result, the present findings on these two-phase nanostructured/amorphous NdPrFe<sub>17</sub> melt-spun ribbons yield to a reinforcement of the refrigerant capacity of the system when Curie temperatures of both phases are close to each other.

In summary, a two-phase composite has been synthesized by melt-spinning procedure in NdPrFe<sub>17</sub> alloys with ribbon geometry. The ribbons exhibit two successive second-order magnetic phase transitions corresponding to the rhombohedral Th<sub>2</sub>Zn<sub>17</sub>-type nanocrystals and a minor amorphous intergranular phase. The dual-magnetic phase character of the system gives rise to a reversible broad magnetic entropy change curve with larger working temperature range and refrigerant capacity around room temperature than that of Pr<sub>2</sub>Fe<sub>17</sub> bulk crystalline counterpart. The use of the melt-spinning technique optimizes the fabrication process avoiding the needed prolonged thermal annealing at high temperatures to produce the 2:17 single-phase crystalline bulk alloys.

This work has been financially supported by: (a) Project Nos. CB-2010-01-156932 and 00232624 (CONACyT, Mexico), and MAT2011-27573-C04 (MINECO, Spain); and (b) Laboratorio Nacional de Investigaciones en Nanociencias y Nanotecnología (LINAN, IPICYT). The technical support received from Dr. G. J. Labrada-Delgado and Dr. H. G. Silva-Pereyra during SEM and TEM observations, respectively, is recognized. C. F. Sánchez-Valdés thanks LINAN, IPICYT, and CONACyT (Project No. CB-2012-01-183770) for supporting his postdoctoral stay.

<sup>1</sup>A. M. Tishin and Y. I. Spichkin, *The Magnetocaloric Effect and its Applications* (IOP Publ., Bristol, 2003).

- <sup>2</sup>K. A. Gschneidner, Jr., V. K. Pecharsky, and A. O. Tsokol, *Rep. Prog. Phys.* **68**, 1479 (2005).
- <sup>3</sup>K. A. Gschneidner, Jr., V. K. Pecharsky, A. O. Pecharsky, and C. B. Zimm, *Mater. Sci. Forum* **315–317**, 69 (1999).
- <sup>4</sup>M. E. Wood and W. H. Potter, *Cryogenics* **25**, 667 (1985).
- <sup>5</sup>K. A. Gschneidner, Jr and V. K. Pecharsky, *J. Appl. Phys.* **85**, 5365 (1999).
- <sup>6</sup>B. Chevalier, J.-L. Bobet, J. Sánchez Marcos, J. Rodríguez Fernández, and J. C. Gómez Sal, *Appl. Phys. A* **80**, 601 (2005).
- <sup>7</sup>P. Gorria, J. L. Sánchez Llamazares, P. Álvarez, M. J. Pérez, J. S. Marcos, and J. A. Blanco, *J. Phys D: Appl. Phys.* **41**, 192003 (2008).
- <sup>8</sup>P. Gorria, P. Álvarez, J. S. Marcos, J. L. S. Llamazares, M. J. Pérez, and J. A. Blanco, *Acta Mater.* **57**, 1724 (2009).
- <sup>9</sup>P. Álvarez, P. Gorria, V. Franco, J. S. Marcos, M. J. Pérez, J. L. Sánchez Llamazares, I. P. Orench, and J. A. Blanco, *J. Phys.: Condens. Matter* **22**, 216005 (2010).
- <sup>10</sup>J. L. Sánchez Llamazares, H. Flores-Zuñiga, C. Sánchez-Valdes, C. A. Ross, and C. García, *J. Appl. Phys.* **111**, 07A932 (2012).
- <sup>11</sup>C. Zimm, A. Jastrab, A. Sternberg, V. K. Pecharsky, K. A. Gschneidner, Jr., M. Osborne, and I. Anderson, *Adv. Cryo. Eng.* **43**, 1759 (1998).
- <sup>12</sup>T. Hashimoto, T. Kuzuhara, M. Sahashi, K. Inomata, A. Tomokiyo, and H. Yayama, *J. Appl. Phys.* **62**, 3873 (1987).
- <sup>13</sup>T. Hashimoto, T. Kuzuhara, M. Sahashi, K. Inomata, A. Tomokiyo, and H. Yayama, *IEEE Trans. Magn.* **23**, 2847 (1987).
- <sup>14</sup>A. Smaïli and R. Chahine, *Adv. Cryo. Eng. Mater.* **42**, 445 (1997).
- <sup>15</sup>A. Smaïli and R. Chahine, *J. Appl. Phys.* **81**, 824 (1997).
- <sup>16</sup>B. J. Korte, K. A. Gschneidner, Jr, and V. K. Pecharsky, *J. Appl. Phys.* **84**, 5677 (1998).
- <sup>17</sup>V. Franco and A. Conde, *Scr. Mater.* **67**, 594 (2012).
- <sup>18</sup>R. Caballero-Flores, V. Franco, A. Conde, K. E. Knippling, and M. A. Willard, *Appl. Phys. Lett.* **98**, 102505 (2011).
- <sup>19</sup>P. Alvarez, J. L. Sánchez Llamazares, P. Gorria, and J. A. Blanco, *Appl. Phys. Lett.* **99**, 232501 (2011).
- <sup>20</sup>S. C. Paticopoulos, R. Caballero-Flores, V. Franco, J. S. Blazquez, A. Conde, K. E. Knippling, and M. A. Willard, *Solid State Commun.* **152**, 1590 (2012).
- <sup>21</sup>P. Álvarez, P. Gorria, J. L. Sánchez Llamazares, and J. A. Blanco, *J. Alloys Compd.* **568**, 98 (2013).
- <sup>22</sup>S. Gorsse, B. Chevalier, and G. Orveillon, *Appl. Phys. Lett.* **92**, 122501 (2008).
- <sup>23</sup>W. Y. Tian, B. H. Yan, P. M. Xiang, Z. DeQian, and W. WeiHua, *Sci. China Ser. G-Phys. Mech. Astron.* **51**, 337 (2008).
- <sup>24</sup>J. Chen, B. G. Schen, Q. Y. Dong, F. X. Hu, and J. R. Sun, *Appl. Phys. Lett.* **95**, 132504 (2009).
- <sup>25</sup>H. Fu, Q. Zheng, and M. X. Wang, *Appl. Phys. Lett.* **99**, 162504 (2011).
- <sup>26</sup>H. Fu, Z. Ma, X. J. Zhang, D. H. Wang, B. H. Teng, and E. A. Balfour, *Appl. Phys. Lett.* **104**, 072401 (2014).
- <sup>27</sup>F. Weitzer, K. Hiebl, and P. J. Rogl, *J. Appl. Phys.* **65**, 4963 (1989).
- <sup>28</sup>J. J. M. Franse and R. J. Radwanski, in *Handbook of Magnetic Materials*, Vol. 7, edited by K. H. J. Buschow (Elsevier Science Publishers B.V., Amsterdam, 1993), p. 307.
- <sup>29</sup>S. Yu. Dankov, V. V. Ivchenko, A. M. Tishin, K. A. Gschneidner, Jr., and V. K. Pecharsky, *Adv. Cryo. Eng. Mater.* **46**, 397 (2000).
- <sup>30</sup>K. Mandal, A. Yan, P. Kersch, A. Handstein, O. Gutfleisch, and K.-H. Müller, *J. Phys. D: Appl. Phys.* **37**, 2628 (2004).
- <sup>31</sup>Y. K. Fang, C. W. Chang, C. C. Yeh, H. W. Chang, W. Li, and W. C. Chang, *J. Appl. Phys.* **103**, 07B302 (2008).
- <sup>32</sup>J. Rodríguez-Carvajal, *Physica B* **192**, 55 (1993).
- <sup>33</sup>P. Álvarez-Alonso, J. L. Sánchez Llamazares, C. F. Sánchez-Valdés, G. J. Cuello, V. Franco, P. Gorria, and J. A. Blanco, *J. Appl. Phys.* **115**, 17A929 (2014).
- <sup>34</sup>E. Brück, *J. Phys. D: Appl. Phys.* **38**, R381 (2005).